

Advanced Molecular Layer Deposition of $\text{Si}_x\text{Zn}_y\text{O}_z$ Thin Film Coatings for Improved Electrochemical Performance of NMC811

Sri Harsha Akella^{+[a]}, Ayan Mukherjee^{+[a]}, Ortal Lidor-Shalev,^{*[a]} Roman Bashkurov,^[b] Yang Wang,^[c] Isaac Buchine,^[e] Longlong Wang,^[a] Melina Zysler,^[a] Michal Ejgenberg,^[a] Tatyana Kravchuk,^[b] Alexander C. Kozen,^[f] Dmitry Bravo-Zhivotovskii,^[b] Yitzhak Apeloig,^[b] Sang Bok Lee,^{*[c]} Xiulin Fan,^{*[g]} Michal Leskes,^{*[e]} and Malachi Noked^{*[a]}

The practical realization of Nickel-rich layered oxide cathode materials such as $\text{LiNi}_{0.8}\text{Mn}_{0.1}\text{Co}_{0.1}\text{O}_2$ (NMC811) is hampered by several structural and interfacial instabilities over prolonged cycling. Several reports have proposed surface passivation via an artificial cathode electrolyte interphase (ACEI) as a promising method for mitigating the parasitic reactions affecting NMC811 while simultaneously improving its electrochemical performance over prolonged cycling. Herein, we report an in-house designed $(\text{tBuMe}_2\text{Si})_2\text{Zn}$ single source precursor for developing $\text{Si}_x\text{Zn}_y\text{O}_z$ ternary CEI thin films on NMC811 via molecular layer deposition (MLD) in combination with O_3 or H_2O as oxidizing agent. We demonstrate that the single precursor $(\text{tBuMe}_2\text{Si})_2\text{Zn}$ avoids the need for two different precursors (Si & Zn). In-depth

spectroscopic studies reveal the mechanism of the formation of organosiloxane/zinc-oxide composite thin film, via intermediates of unprecedented organo-silicon-zinc compounds. Understanding the reaction mechanism paved the path for a successful deposition of ACEI on NMC811. Rate capability studies shows the ACEI protected cathodes exhibit higher discharge capacity at 4 C than pristine NMC811. Furthermore, studies on full cells with graphite anode were conducted to evaluate the practical viability of $\text{Si}_x\text{Zn}_y\text{O}_z$ ACEI thin films on NMC811. After prolonged cycling the ACEI-coated NMC811 full cells significantly improved the electrochemical performance than pristine NMC811 by ~12%.

Introduction

With the ever increasing demand for improved battery performance, there has been significant interest in nickel-rich NMC cathode materials, particularly NMC811 ($\text{LiNi}_{0.8}\text{Mn}_{0.1}\text{Co}_{0.1}\text{O}_2$) owing to its low Cobalt content and high energy density capability.^[1,2] However, nickel-rich NMC811 cathodes suffer several irreversible chemical reactions that occur at the cathode electrolyte interphase (CEI).^[3,4] These reactions are predominantly due to the presence of a large fraction of Ni^{3+} (58%) in NMC811, which is oxidized to Ni^{4+} when in its highly delithiated state.^[5] Consequently, unstable Ni^{4+} is then reduced forming

insulating NiO phases on the NMC811 crystal surface resulting in high interfacial cell impedance and poor cell electrochemical performance.^[6] Furthermore, the release of oxygen from the NMC surface lattice triggers electrolyte decomposition and promotes a phase transition from layered spinel to a rock salt structure on the surface of the NMC811.^[3,4] The HF formed as a byproduct of electrolyte decomposition will dissolve transition metal oxides (i.e. cathode materials), followed by metal ion migration and deposition on the anode side, further accelerating electrolyte decomposition and impedance rise of the cell.^[7,8] Additionally, Nickel rich positive electrode materials are prone to cationic mixing during prolonged cycling; where Ni^{2+} ions

[a] S. H. Akella,⁺ A. Mukherjee,⁺ O. Lidor-Shalev, L. Wang, M. Zysler, M. Ejgenberg, M. Noked
Department of Chemistry, Bar-Ilan University, Ramat Gan, 529002, Israel
and
Bar-Ilan Institute of Nanotechnology and Advanced Materials, Ramat Gan, 529002, Israel
E-mail: Malachi.Noked@biu.ac.il
ortalidor@gmail.com

[b] R. Bashkurov, T. Kravchuk, D. Bravo-Zhivotovskii, Y. Apeloig
Schulich Faculty of Chemistry, Technion-Israel Institute of Technology, Israel

[c] Y. Wang, S. B. Lee
Department of Chemistry and Biochemistry, University of Maryland, College Park, MD 20740 (USA)
E-mail: slee@umd.edu

[e] I. Buchine, M. Leskes
Department of Chemistry, Weizmann Institute of Science, Israel
E-mail: michal.leskes@weizmann.ac.il

[f] A. C. Kozen
Department of Physics, University of Vermont, Burlington VT 05405 (USA)

[g] X. Fan
State Key Laboratory of Silicon Materials, School of Materials Science and Engineering, Zhejiang University, Hangzhou 310027, People's Republic of China
E-mail: xlfan@zju.edu.cn

[+] Equal contribution.

Supporting information for this article is available on the WWW under <https://doi.org/10.1002/batt.202400241>

© 2024 The Authors. Batteries & Supercaps published by Wiley-VCH GmbH. This is an open access article under the terms of the Creative Commons Attribution Non-Commercial License, which permits use, distribution and reproduction in any medium, provided the original work is properly cited and is not used for commercial purposes.

diffuse to occupy vacant Li^+ octahedral sites due to the small difference in ionic radii between Li^+ (0.76 Å) and Ni^{2+} (0.69 Å).^[9,10] Nickel-rich cathode materials also experience anisotropic lattice expansion and contraction upon cycling,^[11] leading to the development of cracks at grain boundaries, compromising the overall structural integrity of the NMC crystal.^[12]

Surface passivation of NMC811 layers has been shown viable to mitigate these parasitic chemical reactions and stabilize the electrochemical performance during prolonged cycling. One promising approach to demonstrate surface protection is vapor-phase deposition of surface coatings.^[13–17] In particular, Atomic layer deposition (ALD) has emerged as an effective method for deposition of these artificial cathode electrolyte interphase (ACEI) coatings, as thin films can be deposited conformally at low temperature with thickness precision at the atomic scale.^[18–20] Initial work has focused on understanding the performance of binary metal oxides: ZrO_2 , Al_2O_3 , WO_3 and MgO because of their high chemical and electrochemical stability. However, the low diffusion rates of Li^+ in these materials result in a drastic decrease in rate or power capability as soon as the coating layer exceeds an optimal thickness level which limits the efficacy of the protection layers.^[21] Interestingly, improved rate capability and prolonged cycling stability can be achieved using passivation layers made of ternary materials such as $\text{Al}_2\text{O}_3\text{-Ga}_2\text{O}_3$ and $\text{Li}_x\text{Sn}_y\text{O}_z$.^[22,23] Nevertheless the inherent complexity in ternary ALD process deposition, processing multielement film from a suitable single-source precursor eliminates the need for multiple sequential reaction steps using separate precursors during a typical ALD process.^[24,25] Recently, we introduced a new family of precursors that enables deposition of multiple elements all originating from a single molecule, which exhibits similarity to molecular layer deposition (MLD) processes.^[26,27] As a proof of concept, Rosy et al. deposited an alkylated $\text{Li}_x\text{Si}_y\text{O}_z$ artificial cathode electrolyte interphase (ACEI) on lithium and manganese rich NCM from a single-source inorganic MLD precursor.^[28,29]

In this work, we explore the deposition chemistry of a new single source precursor; $(t\text{-BuMe}_2\text{Si})_2\text{Zn}$ (alkylated bis(silyl)zinc), which upon oxidation with water or ozone forms a stable surface passivation layer of organosiloxane/zinc-oxide composite ($\text{Si}_x\text{Zn}_y\text{O}_z$) thin film on NMC811 for improved rate performance and prolonged cycling stability. We assert that surface passivation of NMC811 via $\text{Si}_x\text{Zn}_y\text{O}_z$ using $(t\text{-BuMe}_2\text{Si})_2\text{Zn}$ precursor has two-fold advantages: 1. surface passivation of silicon oxide could protect the active material from HF attack,^[30] and 2. Zinc containing oxide coating and Zn^{+2} doping of the cathode surface enhances the structural integrity of the active material thereby stabilizing its electrochemical performance over prolonged cycling.^[24,31]

Herein, we conduct a systematic study on the mechanism of MLD synthesis of $\text{Si}_x\text{Zn}_y\text{O}_z$ thin films using $(t\text{-BuMe}_2\text{Si})_2\text{Zn}$ as a precursor in combination with O_3 or H_2O , and we further examine the effect of these films as ACEI on NMC811. From here onwards, $\text{Si}_x\text{Zn}_y\text{O}_z$ thin films prepared using $(R_3\text{Si})_2\text{Zn}$ and H_2O will be referred to as ' $\text{Si}_x\text{Zn}_y\text{O}_z/\text{H}_2\text{O}$ ', and the coated NMC811 electrode as ' $\text{Si}_x\text{Zn}_y\text{O}_z/\text{H}_2\text{O@NMC811}$ '. Similarly, $\text{Si}_x\text{Zn}_y\text{O}_z$ thin films prepared using $(R_3\text{Si})_2\text{Zn}$ and O_3 will be

referred to as ' $\text{Si}_x\text{Zn}_y\text{O}_z/\text{O}_3$ ', and the coated cathode as ' $\text{Si}_x\text{Zn}_y\text{O}_z/\text{O}_3@\text{NMC811}$ '. In our study we show the oxidation state of silicon in $\text{Si}_x\text{Zn}_y\text{O}_z$ thin film depends on the choice of oxidizing agent (i.e. H_2O or O_3) during the MLD deposition of the thin films. Electrochemical investigation of half cells shows that both ACEI layers stabilize the electrochemical performance of NMC811 during prolonged cycling. Notably, $\text{Si}_x\text{Zn}_y\text{O}_z/\text{H}_2\text{O}@\text{NMC811}$ exhibits higher rate performance than $\text{Si}_x\text{Zn}_y\text{O}_z/\text{O}_3@\text{NMC811}$, which is attributed to improved Li-ion transport through the $\text{Si}_x\text{Zn}_y\text{O}_z/\text{H}_2\text{O}$ @NMC811 ACEI. Furthermore, full-cell studies show that both $\text{Si}_x\text{Zn}_y\text{O}_z/\text{H}_2\text{O}$ and $\text{Si}_x\text{Zn}_y\text{O}_z/\text{O}_3$ improve the capacity retention of NMC811 after prolonged cycling. More significantly, $\text{Si}_x\text{Zn}_y\text{O}_z/\text{H}_2\text{O}$ greatly improves the rate capability with respect to pristine CEI. Such advanced coatings can be employed in high energy lithium-ion batteries (LIB).

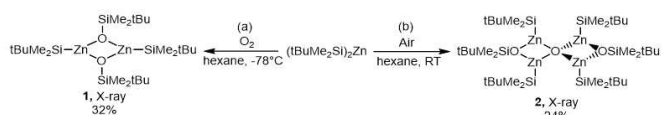
Results and Discussion

Mechanism of $\text{Si}_x\text{Zn}_y\text{O}_z$ growth by MLD from a single-source precursor.

Applett et al. reported that the oxidation or hydrolysis of organozinc compounds such as $(t\text{-BuMe}_2\text{Si})_2\text{Zn}$ forms zinc-oxide bonds, along with various intermediary alkyl(alkoxy)zinc hydroxides and zincoxanes.^[32] We hypothesized that the oxidation and hydrolysis of bis(silyl)zinc under MLD conditions, proceed via similar intermediates containing Si–O and Zn–O bonds, which eventually determine the structure of the $\text{Si}_x\text{Zn}_y\text{O}_z$ thin films. Thus, to obtain a deeper understanding of the structure and properties of the intermediates involved in the formation of $\text{Si}_x\text{Zn}_y\text{O}_z$ thin films, we studied the reaction of bis(silyl)zinc with H_2O , O_2 , or air in a standard Schlenk apparatus.

Reacting $(t\text{-BuMe}_2\text{Si})_2\text{Zn}$ with O_2 at -78°C in hexane produces compound of the formula $[(t\text{-BuMe}_2\text{Si})_2\text{Zn}(\mu\text{-OSi}t\text{BuMe}_2)]_2$ (compound 1) (Scheme 1, path a). Compound 1 was never reported before, and here it was isolated by crystallization from hexane in 32% yield and was then characterized by X-ray crystallography and nuclear magnetic resonance (NMR) spectroscopy (Figure 1, Figures S1–S6). Preliminary X-ray analysis of 1 shows a dimeric $[(t\text{-BuMe}_2\text{Si})_2\text{Zn}(\mu\text{-OSi}t\text{BuMe}_2)]_2$ form featuring bridging siloxy groups and two Si–Zn bonds. The ^{29}Si NMR spectrum of 1 (Figure S6) shows two signals at 0.91 ppm and 15.13 ppm, assigned to the $t\text{-BuMe}_2\text{Si-Zn}$ and $t\text{-BuMe}_2\text{Si-O}$ groups, respectively.

Reacting $(t\text{-BuMe}_2\text{Si})_2\text{Zn}$ with air at room temperature leads to the formation of an additional unreported compound of the formula $[(\text{OSi}t\text{BuMe}_2)_2\text{O}(\mu\text{-ZnSi}t\text{BuMe}_2)_4]$ (compound 2) (Scheme 1, path b). Compound 2 was isolated from hexane in 24% yield and was characterized by NMR spectroscopy (Figures S7–S9) and X-ray crystallography (Figure 1). X-ray



Scheme 1. Reaction of bis(silyl)zinc with O_2 or air.

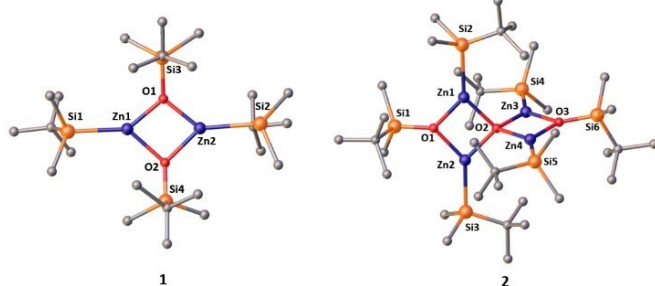


Figure 1. Olex2 drawing of the X-ray crystallographic structures of **1** and **2**. Hydrogen atoms are omitted for clarity. Structural details are given in the Supporting Information (Figures S13 and S14).

molecular analysis of **2** shows a spiro-type structure featuring four Si–Zn bonds and two siloxy groups. The ^{29}Si NMR spectrum of **2** displays two signals at 1.36 ppm and 14.45 ppm, assigned to the tBuMe₂Si–Zn and tBuMe₂Si–O groups, respectively (Figure S9).

On the basis of these observations, we assume that isolated compounds **1** and **2** are the most probable intermediates during the oxidation process of bis(silyl)zinc during the MLD process with ozone. However, we note that ^{29}Si NMR spectroscopy of the reaction mixtures used to synthesize **1** and **2** also shows other peaks, indicating that other products (which we were unable to isolate and fully characterize) are present.

In contrast to the low selectivity of the reaction of (t-BuMe₂Si)₂Zn with O₂ or air (Scheme 1), the reaction of bis(silyl)zinc with H₂O proceeds in a quite selective manner. Thus, the addition of a tetrahydrofuran (THF) solution of H₂O to (t-BuMe₂Si)₂Zn at room temperature yields silylzinc hydroxide (compound **3**) along with t-BuMe₂SiH as a co-product (Scheme 2). Evaporation of all volatiles (including t-BuMe₂SiH) under reduced pressure followed by crystallization from hexane yields colorless crystals of **3**, which was characterized by X-ray crystallography (Figure 2). The X-ray molecular structure of **3** shows a tetrameric cubane [t-BuMe₂SiZn(μ -OH)]₄ in which each of the hydroxy group is μ_3 -bonded to three tBuMe₂SiZn moieties via zinc atoms (Figures S10–S12). The ^{29}Si NMR spectrum of **3** shows a single peak at –1.80 ppm, corresponding to the tBuMe₂Si group bonded to a Zn atom (Figure S12). Compound **3** can be an intermediate on the way to zinc oxides because its decomposition could be driven by proton transfer from ZnOH species to the zinc-bonded silyl group, with

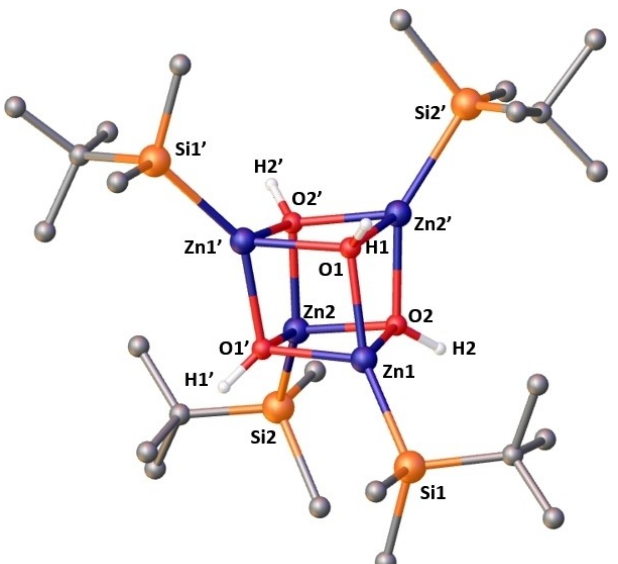
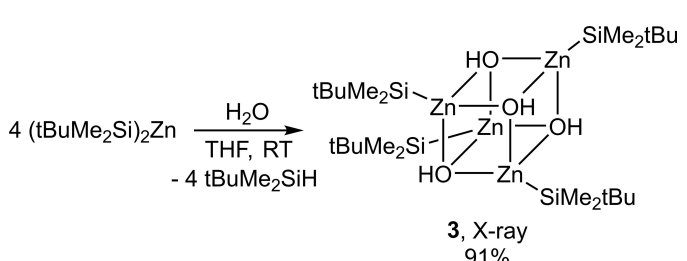


Figure 2. Olex2 drawing of the X-ray crystallographic structures of **3**. Hydrogen atoms on the alkyl substituents are omitted for clarity. Structural details are given in the Supporting Information (Figure S15).

subsequent elimination of a silane. Indeed, zinc hydroxide **3** undergoes decomposition upon thermolysis at 200 °C (the temperature of the MLD process) to produce tBuMe₂SiH and several uncharacterized silicon oxide containing products according to ^{29}Si NMR spectroscopy.

To enable the detection of Si species in the surface thin film synthesized by MLD of (t-BuMe₂Si)₂Zn and H₂O/O₃ we utilized TiO₂ particles as a substrate in the MLD process. The diamagnetic nature and high surface area of TiO₂ particles (in contrast to the strongly paramagnetic NMC substrate) allows us to perform high sensitivity solid state NMR (ssNMR) measurements by utilizing dynamic nuclear polarization (DNP) ^[33]. HRTEM images of the pristine TiO₂ are presented in Figure S16, while Si_xZn_yO_z@TiO₂ and Si_xZn_yO_z/H₂O@TiO₂ are presented in Figure 3(a) and 3(b) respectively. In order to characterize the deposited film, we employed ^1H - ^{29}Si cross polarization (CP) DNP- ssNMR measurements. ^[28] Figure 3 shows the ^1H - ^{29}Si CP DNP ssNMR spectra of thin films obtained by treatment with O₃ (in red) and H₂O (in blue). After ozone treatment, three ^{29}Si resonances were detected at 20, 0, and –40 ppm. After water treatment, these resonances were also observed, but they were accompanied by another low-frequency peak at –75 ppm. The resonances at –40 and –75 ppm can be assigned to different alkylated siloxane groups (probably R₂Si(OSi)₂ or RSi(OSi)₃), whereas the peaks at 0 and 20 ppm could be assigned, on the basis of the comparison with the ^{29}Si NMR spectra of compounds **1**, **2**, and **3** (Figure 4), to Si–Zn and R₃Si–O moieties. Similar spectra were acquired when ^{29}Si nuclei were polarized directly (and not through ^1H CP). This suggests that all Si environments are close to protons or are exposed to the solvent containing the polarizing agent for DNP, resulting in efficient polarization transfer across the coating layer. For a more precise assignment of the ^{29}Si resonances and elucidation of the structure of the thin film layers, further studies are required.



Scheme 2. Reaction of bis(silyl)zinc with H₂O.

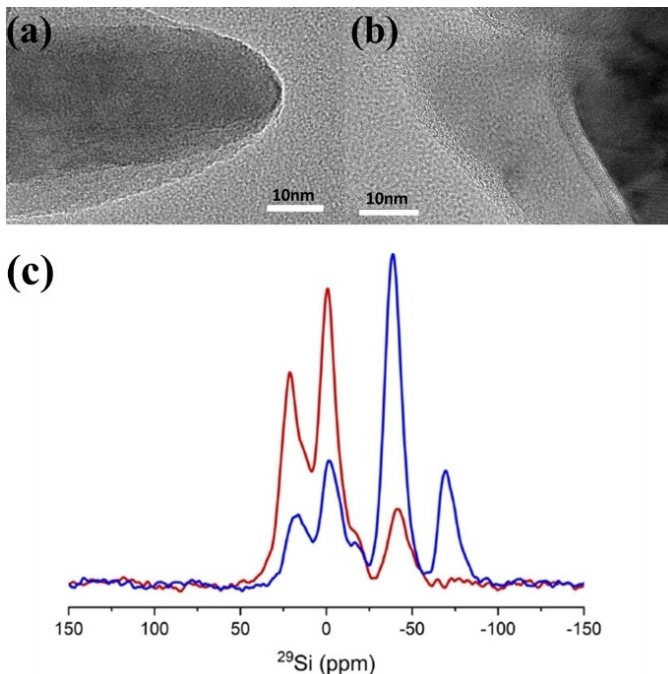


Figure 3. (a) $\text{Si}_x\text{Zn}_y\text{O}_z/\text{O}_3@\text{TiO}_2$, (b) $\text{Si}_x\text{Zn}_y\text{O}_z/\text{H}_2\text{O}@\text{TiO}_2$, (c) ^1H - ^{29}Si CP DNP-ssNMR spectra of the $\text{Si}_x\text{Zn}_y\text{O}_z$ thin films produced by treatment of the bis(silyl)zinc precursor with O_3 (red) and H_2O (blue).

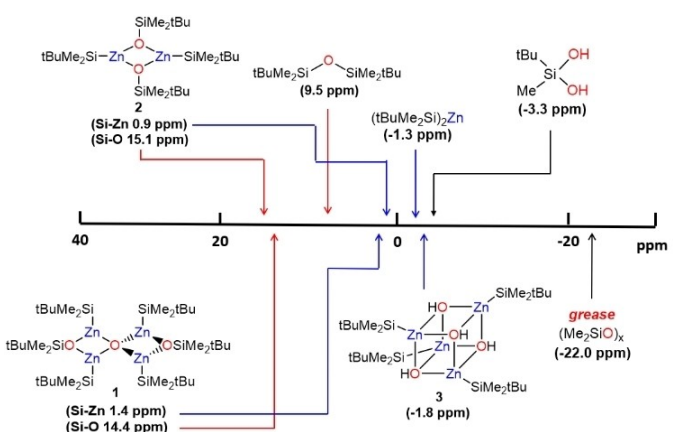


Figure 4. Schematic representation of ^{29}Si NMR chemical shifts of newly synthesized and known silyl compounds.

MLD of the $\text{Si}_x\text{Zn}_y\text{O}_z$ thin films over the NMC811 cathode. The process of MLD coating of NMC811 using $(t\text{-BuMe}_2\text{Si})_2\text{Zn}$ with an O precursor (O_3 or H_2O). To confirm the successful surface coating, transmission electron microscopy (TEM) was conducted. In TEM images of the pristine NMC811 sample (Figure S17) we observed some non-uniform surface impurities which might have originated from the synthesis process of the commercial cathode.^[19] Figure 5a,b shows TEM images of $\text{Si}_x\text{Zn}_y\text{O}_z/\text{O}_3$, $\text{Si}_x\text{Zn}_y\text{O}_z/\text{H}_2\text{O}$ respectively. Figure S17b,c further shows TEM images at higher resolutions. The ALD coated ACEI thin films exhibit conformal coatings nevertheless with varying thickness. The TEM images in Figure S17b,c indicates the $\text{Si}_x\text{Zn}_y\text{O}_z/\text{O}_3$ ACEI thin film to have relatively thicker

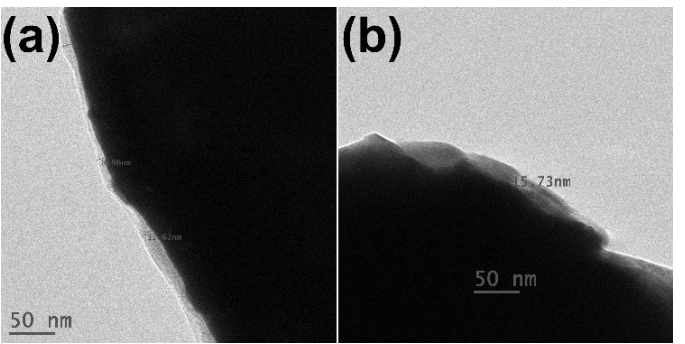


Figure 5. TEM images of (a) $\text{Si}_x\text{Zn}_y\text{O}_z/\text{O}_3@\text{NMC811}$, (b) $\text{Si}_x\text{Zn}_y\text{O}_z/\text{H}_2\text{O}@\text{NMC811}$.

coatings when compared with $\text{Si}_x\text{Zn}_y\text{O}_z/\text{H}_2\text{O}$ ACEI thin film (corresponding to 50 MLD cycles).

X-ray diffraction analysis of pristine NMC811, $\text{Si}_x\text{Zn}_y\text{O}_z/\text{O}_3@\text{NMC811}$, and $\text{Si}_x\text{Zn}_y\text{O}_z/\text{H}_2\text{O}@\text{NMC811}$ was conducted to determine the effect of the MLD coating on the overall layered oxide structure. The diffraction peaks shows that the bulk crystallographic structure of the layered oxide remains unchanged (Figure 6) after MLD treatment with the novel $(t\text{-BuMe}_2\text{Si})_2\text{Zn}$ single-source precursor.

Furthermore, the presence of the coated elements on the surface of the NMC powder was confirmed by inductively coupled plasma elemental analysis. Table S1 shows the silicon and zinc concentrations in the coatings obtained by the two

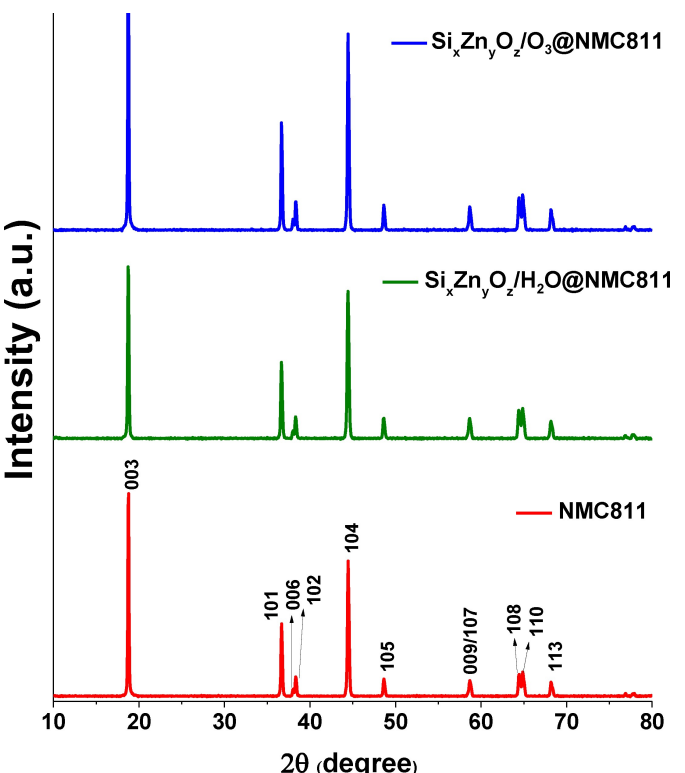


Figure 6. X-ray diffraction spectra of pristine NMC811 (red), $\text{Si}_x\text{Zn}_y\text{O}_z/\text{H}_2\text{O}@\text{NMC811}$ (green), or $\text{Si}_x\text{Zn}_y\text{O}_z/\text{O}_3@\text{NMC811}$ (blue).

different oxidation methods. The presence of the coating is well supported by the ICP results.

X-ray photoelectron spectroscopy (XPS) was conducted to study the chemical environments and oxidation states of the elements in the coatings and in the close to surface transition metals in the NMC811. Figure 7 shows overlays of XPS spectra for C, Zn, and Si in pristine NMC811 and the ACEI-coated NMC811 samples. Figure 7a shows the C 1s spectra (referenced to 284.8 eV) for pristine NMC811 and both $\text{Si}_x\text{Zn}_y\text{O}_z$ -coated NMC811 samples. Table S2 depicts the atomic weight percentages of C 1s of pristine NMC811 and ALD treated samples, in case of the ALD treated samples we clearly see a slight decrease in the atomic percentages of C 1s. Figure 7b presents their Si 2p spectra, where binding energy peaks vary from 101 to 103 eV, demonstrating the presence of SiO_x or Si–O–Zn bonding on both coated samples.^[34,35] Similarly, the Si 2s spectra of the coated samples exhibit active binding energy states close to ~153 eV, demonstrating the presence of Si–O bonds in the material (Figure 7c).^[36–38] These XPS data clearly imply the presence of functionalized siloxane moieties in the $\text{Si}_x\text{Zn}_y\text{O}_z$ thin films.

Generally, we find herein that the oxidation states of the Si in the film grown on the NMC811 cathode surface depends on the nature of the oxygen source used during the MLD reaction. The Si 2p and Si 2s peaks show that Si in the $\text{Si}_x\text{Zn}_y\text{O}_z$ coating has a relatively higher oxidation state when the coating is produced with O_3 than with H_2O ; We assume this is because of pronounced oxidative activity of O_3 during the vapor-phase deposition. Hence, the choice of oxidizing agent between O_3 and H_2O has a major influence on the oxidation state of the Silicon (Si) in the surface thin film coating.^[39] Figure 7d depicts Zn 2p active binding energy states at ~1022.2 and 1044.5 eV, which were attributed to zinc-oxygen bonding in both $\text{Si}_x\text{Zn}_y\text{O}_z$ -coatings.^[24,40,39]

Darapaneni et al. reported that the oxidation state of the transition metals in the cathode surface is influenced by the

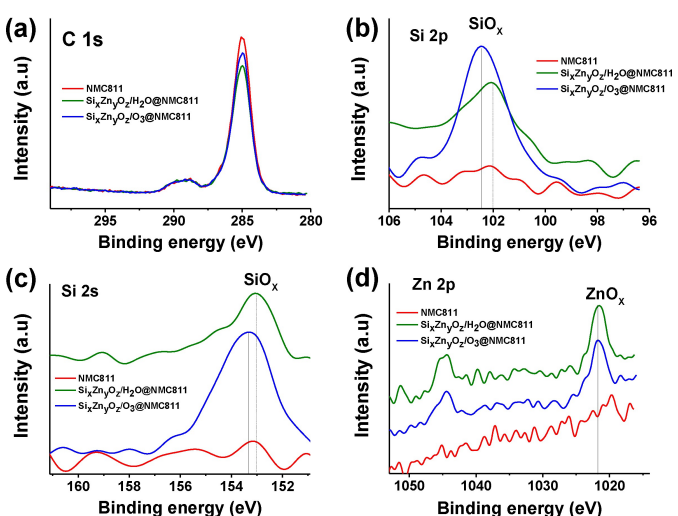


Figure 7. XPS spectra of $\text{Si}_x\text{Zn}_y\text{O}_z/\text{H}_2\text{O}@\text{NMC811}$ (green) and $\text{Si}_x\text{Zn}_y\text{O}_z/\text{O}_3@\text{NMC811}$ (blue) showing peaks of a) C 1s, b) Si 2p, c) Si 2s, and (d) Zn 2p.

nature of the precursor and the produced coating; therefore, further XPS analysis was conducted to characterize the transition metal oxides in the coatings. Figure 8a presents the deconvoluted Ni 2p and O 1s XPS spectra of pristine NMC811, $\text{Si}_x\text{Zn}_y\text{O}_z/\text{O}_3@\text{NMC811}$, and $\text{Si}_x\text{Zn}_y\text{O}_z/\text{H}_2\text{O}@\text{NMC811}$. Pristine NMC811 exhibits a Ni 2p_{3/2} binding energy state at 855.2 eV.^[24,40] The Ni 2p_{3/2} binding energy of $\text{Si}_x\text{Zn}_y\text{O}_z/\text{H}_2\text{O}@\text{NMC811}$ is 0.4 eV lower, indicating a slight reduction in its oxidation state. As for $\text{Si}_x\text{Zn}_y\text{O}_z/\text{O}_3@\text{NMC811}$, its Ni 2p_{3/2} peak is shifted to a higher binding energy by 0.3 eV compared to pristine NMC811. Similar trends were observed in the Co 2p and Mn 2p XPS spectra of pristine NMC811, $\text{Si}_x\text{Zn}_y\text{O}_z/\text{H}_2\text{O}@\text{NMC811}$, and $\text{Si}_x\text{Zn}_y\text{O}_z/\text{O}_3@\text{NMC811}$ (Figure S18). These shifts in the binding energies of the transition metals demonstrate a slight reduction of the surface species on layered oxide NMC811 when H_2O is used as the oxidizing precursor for the MLD.

The O 1s XPS spectra of the three studied samples were then studied to better understand the influence of the oxidizing precursor on the thin film coatings (Figure 8b). The deconvolution of the O 1s peaks of pristine NMC811 reveals peaks at a binding energy of 529.4, 531.3, 531.9, and 532.8 eV, attributed to O-lattice from NMC (namely, R–O–Li), $\text{CO}_2/\text{O}=\text{C=O}$, and M–O–H (LiOH), and other surface impurities, respectively.^[24,38]

For $\text{Si}_x\text{Zn}_y\text{O}_z/\text{H}_2\text{O}@\text{NMC811}$, the O 1s peaks are shifted to a lower binding energy, whereas for $\text{Si}_x\text{Zn}_y\text{O}_z/\text{O}_3@\text{NMC811}$, the O 1s peaks are shifted to a higher binding energy relative to pristine NMC811 (Table S3). These results confirm that the choice between H_2O and O_3 for the MLD has a slight effect on the oxidation states of the species in the coating and the transition metal oxides in the NMC811 near-surface layer.

We have previously reported Zinc penetration in near-surface layers of NMC811 crystal during high temperature vapor

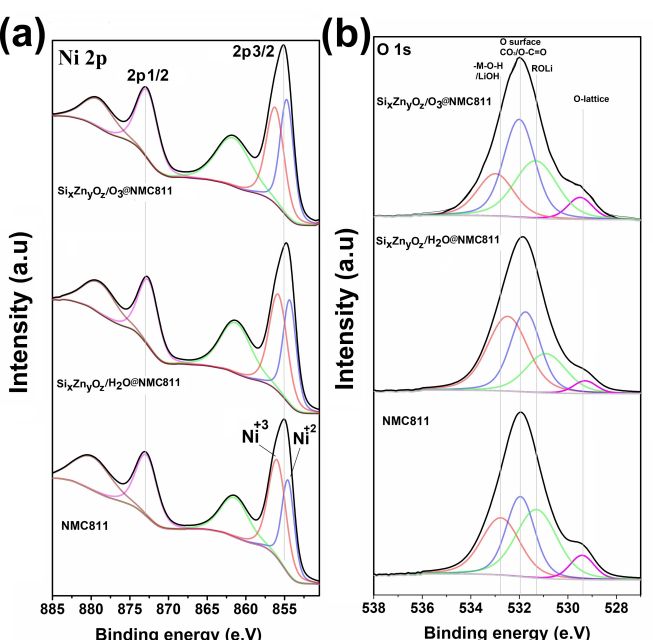


Figure 8. X-ray photoelectron spectra of $\text{Si}_x\text{Zn}_y\text{O}_z/\text{H}_2\text{O}@\text{NMC811}$, $\text{Si}_x\text{Zn}_y\text{O}_z/\text{O}_3@\text{NMC811}$, and pristine NMC811, showing peaks of (a) Ni 2p and (b) O 1s.

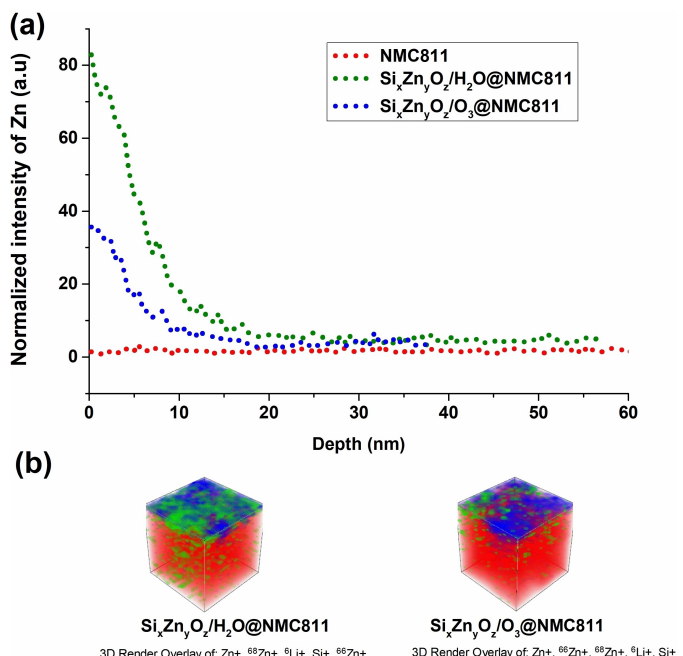


Figure 9. (a) Depth profiles of zinc penetration in the coated NMC811 materials measured by ToF-SIMS (sputter rate of 0.15 nm/sec). Each data point is an average of three identical measurements. (b) 3D renderings of $\text{Si}_x\text{Zn}_y\text{O}_z/\text{H}_2\text{O}$ @NMC811 (left) and $\text{Si}_x\text{Zn}_y\text{O}_z/\text{O}_3$ @NMC811 (right), with Zn (green), Si (blue), and Li (red) ions (the axes scales were changed for better visualization).

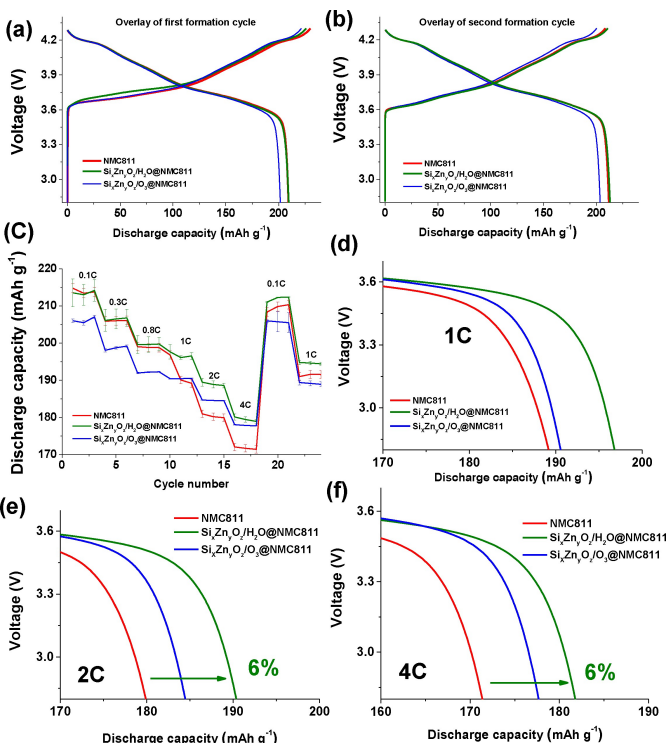


Figure 10. Voltage profiles vs specific discharge capacity of pristine NMC811, $\text{Si}_x\text{Zn}_y\text{O}_z/\text{O}_3$ -NMC811, and $\text{Si}_x\text{Zn}_y\text{O}_z/\text{H}_2\text{O}$ @NMC811: (a) first formation cycle and (b) second formation cycle. (c) Cycling performance at 1 C of pristine NMC811, $\text{Si}_x\text{Zn}_y\text{O}_z/\text{H}_2\text{O}$ @NMC811, and $\text{Si}_x\text{Zn}_y\text{O}_z/\text{O}_3$ @NMC811. Voltage profiles vs specific discharge capacity at (d) 1 C, (e) 2 C, and (f) 4 C.

phase treatment of diethyl zinc on NMC.^[24] Therefore, Time of flight-secondary ion mass spectroscopy (TOF-SIMS) is conducted to reveal the depth penetration ability of Zn^+ during MLD of (*t*BuMe₂Si)₂Zn and O₃ or H₂O as precursors. Figure 9a depicts TOF-SIMS analysis of Zn^+ penetration in ACEI coated NMC811 electrodes. It is observed that $\text{Si}_x\text{Zn}_y\text{O}_z/\text{H}_2\text{O}$ @NMC811 samples have higher Zn^+ penetration when compared to $\text{Si}_x\text{Zn}_y\text{O}_z/\text{O}_3$ @NMC811 samples. Figure 9b,c depicts the 3D visualization images of Zn^+ penetration inside $\text{Si}_x\text{Zn}_y\text{O}_z/\text{H}_2\text{O}$ @NMC811 and $\text{Si}_x\text{Zn}_y\text{O}_z/\text{O}_3$ @NMC811 electrodes.

Electrochemical Performances of $\text{Si}_x\text{Zn}_y\text{O}_z$ -Coated NMC811

Figure 10a,b shows the overlay of first and second formation cycles of pristine NMC811, $\text{Si}_x\text{Zn}_y\text{O}_z/\text{O}_3$ @NMC811, and $\text{Si}_x\text{Zn}_y\text{O}_z/\text{H}_2\text{O}$ @NMC811. The first cycle discharge capacities of pristine NMC811, $\text{Si}_x\text{Zn}_y\text{O}_z/\text{O}_3$ @NMC811 and $\text{Si}_x\text{Zn}_y\text{O}_z/\text{H}_2\text{O}$ @NMC811 are 209.3, 201.5, 209.5 mAh g⁻¹ respectively. During the first cycle charge, $\text{Si}_x\text{Zn}_y\text{O}_z/\text{O}_3$ @NMC811 exhibits slight overpotential behavior at ~3.7 V with respect to pristine NMC811. We attribute phenomenon to impedance from the conformal unlithiated ACEI layer during the initial part of 1st charge cycle, however beyond a voltage of 3.75 V the voltage profile shows no indications of over-voltage, and the phase changes of hexagonal to monoclinic (H1→M) takes place at exactly same voltage for all samples. The overpotential disappears in the following cycles (Figure 10b), which strongly suggests lithiation of the coating eliminated this effect. The phases changes occurring during the formation cycle can be better visualized by differential capacity profiles (Figure S19) during cycling. The oxidation peaks at ≈3.65 to 3.68 V (Figure S19a) in the dQ/dV versus V profiles are attributed to hexagonal (H1) to monoclinic (M) phase (H1↔M) conversion. Further three peaks in dQ/dV profile (at 3.7, 4.01, and 4.19 V, respectively) are attributed to 1) hexagonal to monoclinic (H1↔M); 2) monoclinic to hexagonal (M↔H2) and 3) second hexagonal to third hexagonal (H2↔H3) phase transitions, respectively.^[24,41] Figure S19a depicts early oxidation of $\text{Si}_x\text{Zn}_y\text{O}_z/\text{O}_3$ @NMC811 samples when compared to pristine NMC811 samples. During the second formation cycle (Figure S19b) all the samples followed nearly the same dQ/dV profiles.

Electrochemical studies were conducted for the $\text{Si}_x\text{Zn}_y\text{O}_z/\text{H}_2\text{O}$ @NMC811 and $\text{Si}_x\text{Zn}_y\text{O}_z/\text{O}_3$ @NMC811 samples at various C-rates. The $\text{Si}_x\text{Zn}_y\text{O}_z/\text{O}_3$ @NMC811 samples exhibit poor rate capability till ~1C-rate when compared with pristine NMC811. This is because some coatings impede the rate performance due to poor Li⁺ transport at the ACEI's.^[42–46] Besides the $\text{Si}_x\text{Zn}_y\text{O}_z/\text{H}_2\text{O}$ @NMC811 cathodes exhibits nearly identical discharge capacity as pristine NMC811 till 0.8 C. Notably, at a 1 C rate, $\text{Si}_x\text{Zn}_y\text{O}_z/\text{H}_2\text{O}$ @NMC811 exhibits ~4% higher discharge capacity. More significantly, at higher C-rates, such as 2 C and 4 C, $\text{Si}_x\text{Zn}_y\text{O}_z/\text{H}_2\text{O}$ @NMC811 exhibits ~6% enhancement in discharge capacities with respect to the pristine NMC811. We propose that both $\text{Si}_x\text{Zn}_y\text{O}_z$ coatings improve the discharge capacity of NMC811 at higher rates, particularly $\text{Si}_x\text{Zn}_y\text{O}_z/\text{H}_2\text{O}$, which leads to excellent discharge capacities. We assume that

this phenomenon is the result of greater Zn^{2+} penetration in the near-surface layers of NMC811 in $Si_xZn_yO_z/H_2O@NMC811$ than in $Si_xZn_yO_z/O_3@NMC811$ (Figure 9). Therefore, we propose that greater Zn^{2+} penetration, along with the presence of silioxane moieties in the ACEI, leads to excellent Li-ion transport at the electrode–electrolyte interphase and simultaneously suppresses the parasitic reactions associated with high C-rates.

GITT measurements were conducted to understand the Li-ion transport at the ACEI layer of the electrodes.^[47–49] Figure S20 shows the Li-ion diffusivity coefficient during the charging and discharging of pristine NMC811 and ACEI-coated NMC811. The plots clearly show that Li-ion transport in $Si_xZn_yO_z/H_2O-NMC811$ is similar to that in pristine NMC811. However, $Si_xZn_yO_z/O_3-NMC811$ exhibits relatively poor Li-ion transport which can be due to thicker ACEI layer. As a result, $Si_xZn_yO_z/O_3-NMC811$ samples exhibit poor discharge capacities at low C-rates ($\sim 0.8C$) when compared to that in $Si_xZn_yO_z/H_2O-NMC811$. However, at high C-rate such as 4 C, parasitic reactions become inevitable, leading to the deposition of organic/inorganic layers, such as LiF, on the pristine NMC811, thereby hindering Li-ion transport.^[50,51] In this regard, $Si_xZn_yO_z$ -containing ACEI layers prove beneficial by facilitating excellent Li-ion transport. Notably, $Si_xZn_yO_z/O_3-NMC811$ samples exhibit $\sim 4\%$ discharge capacity enhancement at 4C-rate, while $Si_xZn_yO_z/H_2O-NMC811$ samples exhibit a more substantial $\sim 6\%$ discharge capacity enhancement.

Prolonged electrochemical stability studies (Figure S21a) were conducted for pristine NMC811 and ACEI-coated NMC811 in half cells. Upon prolonged cycling, pristine NMC811 undergoes a gradual decline in discharge capacity, owing to the combination of several parasitic reactions. After 100 cycles, pristine NMC811 retains $\sim 85\%$ of its capacity, whereas $Si_xZn_yO_z/O_3@NMC811$ retains $\sim 86.5\%$ and $Si_xZn_yO_z/H_2O@NMC811$ retains $\sim 88\%$. Upon increasing the discharge rate to 2C-rate, the pristine NMC811 cathodes undergo a steep decline in discharge capacity, which is attributed to combination of several interfacial parasitic reactions on the cathode, such as electrolyte decomposition, phase transition, microcrack formation, and transition metal dissolution.^[11,19,52] After prolonged cycling (200 cycles), pristine NMC811 retains only 52% of its capacity, whereas $Si_xZn_yO_z/H_2O@NMC811$ and $Si_xZn_yO_z/O_3@NMC811$ both retain approximately 72.5%. This shows that the proposed ACEI coating mitigates parasitic reactions and significantly improves the electrochemical properties of NMC811. Further mean voltage plots are analyzed to calculate the round trip efficiency from the difference between the lithiation and delithiation mean voltages, i.e. the voltage hysteresis.^[46,53]

Figure S21b shows the mean voltage of discharge and charge as a function of cycle number for pristine NMC811 and ACEI-coated NMC811s. For the first 100 cycles, at 1C-rate discharge, the three electrodes demonstrated similar round-trip efficiencies. Further cycling at a 2C-rate discharge results in increase of voltage hysteresis for pristine NMC811, but a significantly lower effect for both ACEI-coated NMC811 cathodes: after 200 charge-discharge cycles, the differences between the charge and discharge mean voltages of NMC811

and the ACEI-coated NMC811 cathodes are 427 mV and ~ 348 mV, respectively. This clearly confirms that the ACEI coating mitigates the parasitic reactions in NMC811-based half cells and improves their electrochemical performance. In general, the interpretation of capacity retention in full cell is challenging when the areal capacity is relatively high, due to the degradation of the anode/electrolyte interphase, we therefore conducted additional in-depth studies in full cells (below).

To evaluate the effect of the ACEI in a practical environment, electrochemical studies were further conducted in full cells with graphite anode. Figure 11a presents the overlay of first formation cycles of pristine NMC811, $Si_xZn_yO_z/H_2O@NMC811$, and $Si_xZn_yO_z/O_3@NMC811$ full cells. The voltage profiles of pristine NMC811 full cell depicts voltage plateaus indicating various stages of lithiation on the graphite anode and corresponding delithiation of NMC811 (Figure S22).^[54] ACEI-coated NMC811 full cells exhibit similar charging voltage plateaus, albeit with a slightly smaller overpotential of ~ 4.1 V in all the formation cycles with respect to pristine NMC811 full cells. The minimization of this charging overpotential is more

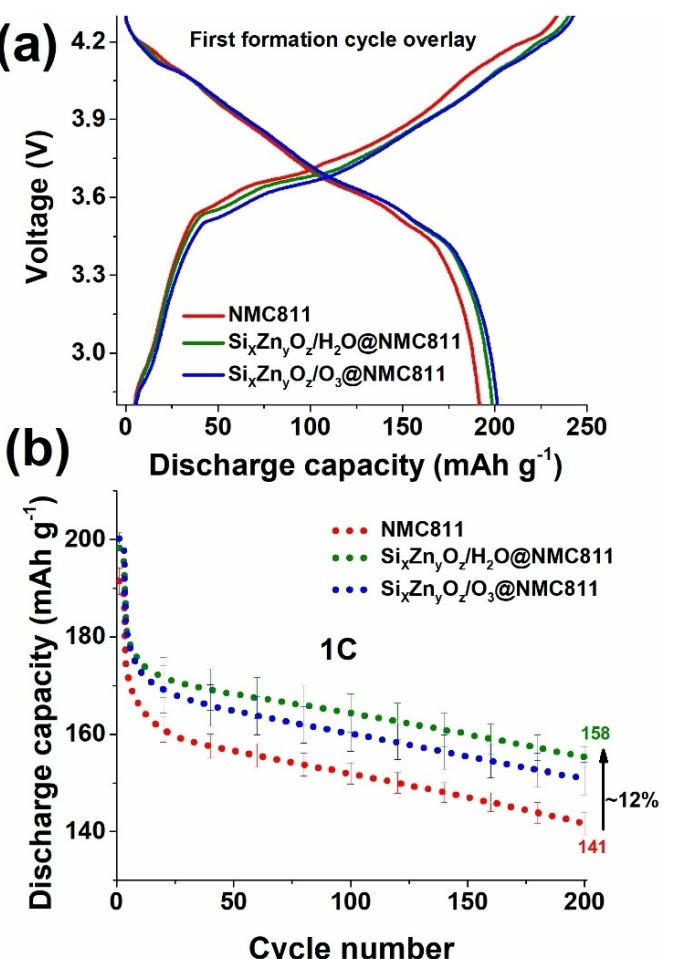


Figure 11. (a) Overlayed full-cell formation cycles of pristine NMC811, $Si_xZn_yO_z/H_2O@NMC811$, and $Si_xZn_yO_z/O_3@NMC811$ and (b) Discharge capacity profiles of pristine NMC811, $Si_xZn_yO_z/H_2O@NMC811$, and $Si_xZn_yO_z/O_3@NMC811$ at 0.5C-rate charge 1C-rate discharge after 3 formation cycles at 0.05C-rate.

clearly identifiable in the differential capacity dQ/dV profiles as a function of the cell potential, V . Figure S23 clearly shows that the differential capacity profiles are more flattened after ~ 4.1 V for the ACEI coated samples than for the pristine NMC811 full cell. This implies that parasitic reactions occurring beyond ~ 4.1 V, such as electrolyte decomposition, are suppressed by the ACEI coating. The pristine NMC811 full cell continues to exhibit relatively higher overpotential in all the formation cycles, implying unstable CEI formation during cycling that doesn't suppress the interfacial parasitic reactions.

The pristine NMC811 full cells yields ~ 191 mAh g $^{-1}$ discharge capacity after the first formation charge (Figure 11a, Figure S22). The relatively low discharge capacity is attributed to the formation of a surface film during delithiation from NMC811 that pushes the voltage to higher value due to increased impedance, and suppression of the delithiation process during charge. The $\text{Si}_x\text{Zn}_y\text{O}_z/\text{O}_3@\text{NMC811}$ full cell yields a discharge capacity of ~ 201.4 mAh g $^{-1}$ and $\text{Si}_x\text{Zn}_y\text{O}_z/\text{H}_2\text{O}@\text{NMC811}$ yields ~ 199 mAh g $^{-1}$. Their improved discharge capacities in case of ACEI coated NMC811 samples is attributed for the suppression of parasitic reactions at the interphases, and decreased overpotential for delithiation process. This phenomenon is clearly observed in the shift of position of the H2-H3 peak in case of pristine NMC811 when compared ACEI-coated NMC811 (Figure S22).^[55,56]

After the formation cycles, the full cells were cycled at 0.5 C charge and 1 C discharge rates (Figure 11b). At 5th cycle the discharge capacity of pristine NMC811 is 171 mAh g $^{-1}$ while both $\text{Si}_x\text{Zn}_y\text{O}_z/\text{O}_3@\text{NMC811}$, $\text{Si}_x\text{Zn}_y\text{O}_z/\text{H}_2\text{O}@\text{NMC811}$ exhibit ~ 183 mAh g $^{-1}$ discharge capacity (Figure 11b, Figure S24a–c).

We assume the severe capacity (lithium) loss incase of pristine NMC811 cells are due to parasitic reactions and SEI thickening on the graphite anode during cycling. In this regard, ACEI coated NMC811 samples improved the capacity retentions. The overlayed coulombic efficiency profiles of pristine NMC811 and ACEI coated NMC811 samples (Figure S24d) further confirm the improved electrochemical performances. At 20th cycle pristine NMC811 yields 156.4 mAh g $^{-1}$ whereas $\text{Si}_x\text{Zn}_y\text{O}_z/\text{O}_3@\text{NMC811}$, $\text{Si}_x\text{Zn}_y\text{O}_z/\text{H}_2\text{O}@\text{NMC811}$ exhibit 174,176 mAh g $^{-1}$ respectively. After 200 cycles pristine NMC811 full cells exhibit ~ 141 mAh/g $^{-1}$ discharge capacity, $\text{Si}_x\text{Zn}_y\text{O}_z/\text{O}_3@\text{NMC811}$ full cells yield 159.3 mAh g $^{-1}$ and $\text{Si}_x\text{Zn}_y\text{O}_z/\text{H}_2\text{O}@\text{NMC811}$ full cells yield 158 mAh g $^{-1}$ (Figure 11b, Figure S24). This implies a remarkable $\sim 12\%$ improved capacity retentions in case of ACEI coated NMC811 cells when compared with pristine NMC811 cells.

Post cycling imedance studies were conducted to further confirm suppression of impedance build-up in case of ACEI-coated NMC811 full cells. Figure S25a depicts the overlayed Nyquist plots of pristine NMC811, $\text{Si}_x\text{Zn}_y\text{O}_z/\text{O}_3@\text{NMC811}$ and $\text{Si}_x\text{Zn}_y\text{O}_z/\text{H}_2\text{O}@\text{NMC811}$ full cells after 200 charge-discharge cycles. The Nyquist plot is composed of two semicircles and an inclined line attributed to the surface film (R_{sl}), charge transfer (R_{ct}), and Warburg resistance, respectively.^[57] Figure S25b shows the equivalent circuit model used for deconvoluting R_{sl} and R_{ct} values using Zview software. The R_{sl} values of pristine NMC811, $\text{Si}_x\text{Zn}_y\text{O}_z/\text{O}_3@\text{NMC811}$ and $\text{Si}_x\text{Zn}_y\text{O}_z/\text{H}_2\text{O}@\text{NMC811}$ full cells are

7.6 Ω , 5.3 Ω and 4.2 Ω respectively (Figure S25c). The R_{ct} values of pristine NMC811, $\text{Si}_x\text{Zn}_y\text{O}_z/\text{O}_3@\text{NMC811}$ and $\text{Si}_x\text{Zn}_y\text{O}_z/\text{H}_2\text{O}@\text{NMC811}$ full cells are 17.4 Ω , 12 Ω and 12 Ω respectively (Figure S25d). The R_{sl} and R_{ct} values are direct implications of suppressed impedance build-up and improved Li-ion kinetics for ACEI-coated NMC811 full cells when compared with pristine NMC811 after 200 cycles. This study further confirms that the ACEI-protected NMC811 samples improve the electrochemical performance of NMC811 while mitigating the parasitic reactions over prolonged cycling.

To deconvolute the origin of parasitic reactions in the full cells postmortem analysis is conducted for manganese dissolution and its deposition on the graphite electrodes. Figure S26 depicts the histogram of the Mn dissolution in pristine NMC811 full cell and ACEI protected full cells. ICP-OES analysis shows ~ 168 ppm of Mn dissolution on the graphite anode against Pristine NMC811 whereas it is ~ 144 ppm and ~ 99 ppm in case of graphite anode against $\text{Si}_x\text{Zn}_y\text{O}_z/\text{O}_3@\text{NMC811}$ and $\text{Si}_x\text{Zn}_y\text{O}_z/\text{H}_2\text{O}@\text{NMC811}$ full cells, respectively. We therefore conclude that part of the severe capacity fade in pristine NMC811 full cells is due to shuttling of manganese into the SEI layer, which leads to increased impedance of the cell and lower efficiency.^[58] This phenomenon is suppressed in case of ACEI protected NMC811 full cells with respect to pristine NMC811 full cells.

Further postmortem HRSEM analysis was conducted on the cycled NMC electrodes to study the intergranular cracking accompanied because of parasitic reactions occurring at the CEI, such as electrolyte decomposition, surface phase transition, and transition metal dissolution.^[6,12,59–66] Figure S27 shows images of the pristine and ACEI-coated NMC811 cycled electrodes. The cycled pristine NMC811 shows severe microcrack propagation due to severe parasitic reactions. In contrast, the ACEI-coated NMC811 electrodes, these parasitic reactions are greatly mitigated, resulting in reduced intergranular cracking. Furthermore, these electrodes are subjected to postmortem TEM analysis (Figure S28). Figure S28a presents a thin layer film on pristine NMC811 indicating the cathode electrolyte interphase formed due to electrolyte decomposition while operating at higher voltages and long-term cycling. While TEM images of $\text{Si}_x\text{Zn}_y\text{O}_z/\text{O}_3@\text{NMC811}$ (Figure S28b) and $\text{Si}_x\text{Zn}_y\text{O}_z/\text{H}_2\text{O}@\text{NMC811}$ (Figure S28c) samples show a thicker layers which we assume to be the retained ACEI thin films on NMC811. Post cycling impedance, manganese dissolution and microscopic imaging studies confirm that the proposed organosiloxane/zinc-oxide composite thin film coatings suppresses parasitic reactions on NMC811 and stabilizes its overall mechanical integrity upon prolonged cycling.

Table S4 present's the comparison of electrochemical improvements of previously reported metal-oxide ACEI thin films on layered oxide cathode materials from our group. The $\text{Si}_x\text{Zn}_y\text{O}_z$ ACEI thin films exhibits nearly same percentage improvement with respect to lithiated ACEI thin films ($\text{Li}_x\text{Si}_y\text{O}_z/\text{Li}_x\text{Sn}_y\text{O}_z$) i.e, $\sim 20\%$. To evaluate the stabilization behaviour, we further coated $\text{Si}_x\text{Zn}_y\text{O}_z$ ACEI on inhouse synthesized Lithium Nickel oxide (LNO)^[67] cathodes. Figure S29a,b depicts the overlayed formation cycles and prolonged cycling stability respectively for pristine LNO and $\text{Si}_x\text{Zn}_y\text{O}_z/\text{H}_2\text{O}@\text{LNO}$ cells. The

$\text{Si}_x\text{Zn}_y\text{O}_z/\text{H}_2\text{O}$ @LNO improves the capacity retentions by great margin of ~36% with compared with pristine LNO cathode upon prolonged cycling (Figure S29). This study further confirms the ability of $\text{Si}_x\text{Zn}_y\text{O}_z$ ACEI thin film can significantly stabilize the electrochemical properties of NMC811 and LNO cathode materials while suppressing the parasitic chemical reactions during prolonged cycling.

Conclusions

In this work, we demonstrated a new ternary MLD processes using the single-source precursor (tBuMe_2Si)₂Zn and O₃ or H₂O as an oxidizing agent to synthesize ACEI thin films consisting of organosiloxane/zinc-oxide composites on NMC811. Spectroscopy studies suggest that the choice between O₃ and H₂O as the oxidizing MLD precursor is dictating the reaction mechanism of the MLD, and therefore the oxidation state and chemical composition of the resulting ACEI thin films. Furthermore, it can also slightly modify the oxidation state of the transition metal oxides of the NMC811 substrate. The $\text{Si}_x\text{Zn}_y\text{O}_z$ ACEI thin films were fully characterized to show that the MLD process can conformally coat NMC811 particles. Galvanostatic measurements revealed that electrochemical performance at 4 C was improved by 4% and 6% for $\text{Si}_x\text{Zn}_y\text{O}_z/\text{O}_3$ @NMC811 and $\text{Si}_x\text{Zn}_y\text{O}_z/\text{H}_2\text{O}$ @NMC811, respectively, compared to uncoated NMC811.

We ascribe the higher discharge capacity of $\text{Si}_x\text{Zn}_y\text{O}_z/\text{H}_2\text{O}$ @NMC811 at 4 C to improved Li-ion transport through the ACEI, an improvement which we attribute the greater zinc penetration in $\text{Si}_x\text{Zn}_y\text{O}_z/\text{H}_2\text{O}$ @NMC811 than in $\text{Si}_x\text{Zn}_y\text{O}_z/\text{O}_3$ @NMC811. After prolonged cycling (200 cycles) at high discharge cycling rates in half cells, the ACEI-coated samples exhibit 20% higher capacity retention than pristine NMC811 electrodes, while in a full cell configuration with graphite anodes the ACEI coatings improve the electrochemical performance of NMC811 by ~12%.

These results demonstrate the practical viability of the thin-film surface passivation of NMC811 using a single precursor to deliver multiple elements in a composite MLD film, while the organosiloxane/zinc-oxide composite thin film improves the electrochemical performance of NMC811 and could ultimately result in improved electrochemical performance of Li-ion batteries.

Experimental Section

Detailed experimental and characterizations are described in the supporting information.

Acknowledgements

The research was supported by the Weizmann Institute Sustainability and Energy Research Initiative and the Israel Science Foundation (grant/08517 to ML and 3494/21 for MN)

and ISF-NSFC (# for MN and XF). UMD and BIU teams acknowledge the BIRD energy center for supporting the collaborative work under UISEC consortium. All authors from BIU thank Israel National institute of Energy storage.

Conflict of Interests

The authors declare that they have no known competing financial interests or personal relationships that could have appeared to influence the work reported in this paper.

Data Availability Statement

The data that support the findings of this study are available from the corresponding author upon reasonable request.

Keywords: MLD • NMC811 • Improved electrochemical performance • ACEI thin films • organosiloxane/zinc-oxide coatings

- [1] W. T. Mujeeb Khan, Muhammed Nawaz Tahir, Syed Farooq Adil, Hadayat Ullah Khan, M. Rafiq, H. Siddiqui, Abdulrahman A. Al-warthan, *J. Mater. Chem. A* **2015**, *12*.
- [2] O. Gröger, H. A. Gasteiger, J.-P. Suchsland, *J. Electrochem. Soc.* **2015**, *162*, A2605.
- [3] G. Assat, J.-M. Tarascon, *Nat. Energy* **2018**, *3*, 373–386.
- [4] T. Li, X.-Z. Yuan, L. Zhang, D. Song, K. Shi, C. Bock, *Electrochem. Energy Rev.* **2020**, *3*, 43–80.
- [5] H. Sun, K. Zhao, *J. Phys. Chem. C* **2017**, *121*, 6002–6010.
- [6] Y.-K. Sun, S.-T. Myung, B.-C. Park, J. Prakash, I. Belharouak, K. Amine, *Nat. Mater.* **2009**, *8*, 320–324.
- [7] D. R. Gallus, R. Schmitz, R. Wagner, B. Hoffmann, S. Nowak, I. Cekic-Laskovic, R. W. Schmitz, M. Winter, *Electrochim. Acta* **2014**, *134*, 393–398.
- [8] I. Buchberger, S. Seidlmayer, A. Pokharel, M. Piana, J. Hattendorff, P. Kudejova, R. Gilles, H. A. Gasteiger, *J. Electrochem. Soc.* **2015**, *162*, A2737.
- [9] H. H. Li, N. Yabuuchi, Y. S. Meng, S. Kumar, J. Breger, C. P. Grey, Y. Shao-Horn, *Chem. Mater.* **2007**, *19*, 2551–2565.
- [10] T. Kawaguchi, K. Fukuda, K. Tokuda, M. Sakaida, T. Ichitsubo, M. Oishi, E. Matsubara, *Phys. Chem. Chem. Phys.* **2015**, *17*, 14064–14070.
- [11] C. Xu, K. Märker, J. Lee, A. Mahadevogowda, P. J. Reeves, S. J. Day, M. F. Groh, S. P. Emge, C. Ducati, B. L. Mehdi, *Nat. Mater.* **2021**, *20*, 84–92.
- [12] H. Liu, M. Wolf, K. Karki, Y.-S. Yu, E. A. Stach, J. Cabana, K. W. Chapman, P. J. Chupas, *Nano Lett.* **2017**, *17*, 3452–3457.
- [13] J. Cho, Y. J. Kim, B. Park, *Chem. Mater.* **2000**, *12*, 3788–3791.
- [14] Z. R. Zhang, H. S. Liu, Z. L. Gong, Y. Yang, *J. Power Sources* **2004**, *129*, 101–106.
- [15] R. A. House, U. Maitra, L. Jin, J. G. Lozano, J. W. Somerville, N. H. Rees, A. J. Naylor, L. C. Duda, F. Massel, A. V. Chadwick, *Chem. Mater.* **2019**, *31*, 3293–3300.
- [16] N. Zhang, N. Zaker, H. Li, A. Liu, J. Inglis, L. Jing, J. Li, Y. Li, G. A. Botton, J. R. Dahn, *Chem. Mater.* **2019**, *31*, 10150–10160.
- [17] Z. Chen, Y. Qin, K. Amine, Y.-K. Sun, *J. Mater. Chem.* **2010**, *20*, 7606–7612.
- [18] W. Li, D. Cheng, R. Shimizu, Y. Li, W. Yao, G. Raghavendran, M. Zhang, Y. S. Meng, *Energy Storage Mater.* **2022**, *49*, 77–84.
- [19] S. H. Akella, S. Taragin, Y. Wang, H. Aviv, A. C. Kozen, M. Zysler, L. Wang, D. Sharon, S. B. Lee, M. Noked, *ACS Appl. Mater. Interfaces* **2021**.
- [20] D. Mohanty, K. Dahlberg, D. M. King, L. A. David, A. S. Sefat, D. L. Wood, C. Daniel, S. Dhar, V. Mahajan, M. Lee, *Sci. Rep.* **2016**, *6*, 26532.
- [21] M. Wolff, S. Lobe, C. Dellen, S. Uhlenbruck, C. Ribeiro, X. H. Guichard, M. Niederberger, A. Makvandi, M. Peterlechner, G. Wilde, *Nano Sel.* **2021**, *2*, 146–157.
- [22] A. Saha, O. Shalev, S. Maiti, L. Wang, S. H. Akella, B. Schmerling, S. Targin, M. Tkachev, X. Fan, M. Noked, *Mater. Today Energy* **2023**, *31*, 101207.

- [23] M. R. Laskar, D. H. K. Jackson, Y. Guan, S. Xu, S. Fang, M. Dreibelbis, M. K. Mahanthappa, D. Morgan, R. J. Hamers, T. F. Kuech, *ACS Appl. Mater. Interfaces* **2016**, *8*, 10572–10580.
- [24] A. Saha, S. Taragin, S. Maiti, T. Kravchuk, N. Leifer, M. Tkachev, M. Noked, *Small* **2022**, *18*, 2104625.
- [25] Y. Zhao, M. Amirmaleki, Q. Sun, C. Zhao, A. Codirenzi, L. V. Goncharova, C. Wang, K. Adair, X. Li, X. Yang, *Matter* **2019**, *1*, 1215–1231.
- [26] E. Kazヤk, M. Shin, W. S. LePage, T. H. Cho, N. P. Dasgupta, *Chem. Commun.* **2020**, *56*, 15537–15540.
- [27] H. Wang, K. E. Gregorczyk, S. B. Lee, G. W. Rubloff, C.-F. Lin, *J. Phys. Chem. C* **2020**, *124*, 6830–6837.
- [28] S. Haber, E. Evenstein, A. Saha, O. Brontvein, Y. Kratish, D. Bravo-Zhitovskii, Y. Apeloig, M. Leskes, M. Noked, *Energy Storage Mater.* **2020**, *33*, 268–275.
- [29] S. Haber, Rosy, A. Saha, O. Brontvein, R. Carmieli, A. Zohar, M. Noked, M. Leskes, *J. Am. Chem. Soc.* **2021**, *143*, 4694–4704.
- [30] Y. Fan, J. Wang, Z. Tang, W. He, J. Zhang, *Electrochim. Acta* **2007**, *52*, 3870–3875.
- [31] A. Sharma, A. Rajkamal, S. Kobi, B. S. Kumar, A. K. Paidi, A. Chatterjee, A. Mukhopadhyay, *ACS Appl. Mater. Interfaces* **2021**, *13*, 25836–25849.
- [32] A. Apblett, A. Barron, A. F. Hepp, *Nanomaterials via Single-Source Precursors: Synthesis, Processing and Applications*, Elsevier, 2022.
- [33] A. J. Rossini, A. Zagdoun, M. Lelli, A. Lesage, C. Copéret, L. Emsley, *Acc. Chem. Res.* **2013**, *46*, 1942–1951.
- [34] J. E. Coyle, M. T. Brumbach, G. M. Veith, C. A. Apblett, *J. Phys. Chem. C* **2020**, *124*, 8153–8161.
- [35] S. C. Ray, D. K. Mishra, A. M. Strydom, P. Papakonstantinou, *J. Appl. Phys.* **2015**, *118*, 115302.
- [36] Y. J. Choi, S.-J. Won, H.-S. Jung, S. Park, D.-Y. Cho, C. S. Hwang, T. J. Park, H. J. Kim, *ECS Solid State Lett.* **2012**, *1*, N4.
- [37] H.-P. Ma, J.-H. Yang, J.-G. Yang, L.-Y. Zhu, W. Huang, G.-J. Yuan, J.-J. Feng, T.-C. Jen, H.-L. Lu, *Nanomaterials* **2019**, *9*, 55.
- [38] D. A. Zatsepin, A. F. Zatsepin, D. W. Boukhvalov, N. V. Gavrilov, *J. Alloys Compd.* **2020**, *829*, 154459.
- [39] P. Darapaneni, A. U. Mane, A. Turczynski, J. W. Elam, *Chem. Mater.* **2021**.
- [40] Rosy, S. Taragin, E. Evenstein, S. Maletti, D. Mikhailova, M. Noked, *ACS Appl. Mater. Interfaces* **2021**, *13*, 44470–44478.
- [41] C. S. Yoon, D.-W. Jun, S.-T. Myung, Y.-K. Sun, *ACS Energy Lett.* **2017**, *2*, 1150–1155.
- [42] Y. Zhu, N. Zhang, L. Zhao, J. Xu, Z. Liu, Y. Liu, J. Wu, F. Ding, *J. Alloys Compd.* **2019**, *811*, 152023.
- [43] M. R. Laskar, D. H. K. Jackson, S. Xu, R. J. Hamers, D. Morgan, T. F. Kuech, *ACS Appl. Mater. Interfaces* **2017**, *9*, 11231–11239.
- [44] M. J. Herzog, N. Gauquelin, D. Esken, J. Verbeeck, J. Janek, *Energy Technol.* **2021**, *9*, 2100028.
- [45] S. H. Akella, S. Taragin, A. Mukherjee, O. Lidor-Shalev, H. Aviv, M. Zysler, D. Sharon, M. Noked, *J. Electrochem. Soc.* **2021**, *168*, 80543.
- [46] J. Cabana, L. Monconduit, D. Larcher, M. R. Palacin, *Adv. Mater.* **2010**, *22*, E170–E192.
- [47] W. Weppner, R. A. Huggins, *J. Electrochem. Soc.* **1977**, *124*, 1569.
- [48] K. Märker, P. J. Reeves, C. Xu, K. J. Griffith, C. P. Grey, *Chem. Mater.* **2019**, *31*, 2545–2554.
- [49] F. N. Sayed, M. B. Sreedhara, A. Soni, U. Bhat, R. Datta, A. J. Bhattacharya, C. N. R. Rao, *Mater. Res. Express* **2019**, *6*, DOI 10.1088/2053-1591/ab3e19.
- [50] D. Aurbach, K. Gamolsky, B. Markovsky, G. Salitra, Y. Gofer, U. Heider, R. Oesten, M. Schmidt, *J. Electrochem. Soc.* **2000**, *147*, 1322.
- [51] S. A. Freunberger, Y. Chen, Z. Peng, J. M. Griffin, L. J. Hardwick, F. Bardé, P. Novák, P. G. Bruce, *J. Am. Chem. Soc.* **2011**, *133*, 8040–8047.
- [52] R. Jung, M. Metzger, F. Maglia, C. Stinner, H. A. Gasteiger, *J. Phys. Chem. Lett.* **2017**, *8*, 4820–4825.
- [53] L. Li, R. Jacobs, P. Gao, L. Gan, F. Wang, D. Morgan, S. Jin, *J. Am. Chem. Soc.* **2016**, *138*, 2838–2848.
- [54] M. B. Pinson, M. Z. Bazant, *ECS Meet. Abstr.* **2013**, MA2013-01, 405.
- [55] K. Kongswatvoragul, P. Bunyanidhi, C. Jangsan, W. Tejangkura, M. Sawangphruk, *J. Electrochem. Soc.* **2022**, *169*, 90524.
- [56] P. J. West, C. D. Quilty, Z. Wang, S. N. Ehrlich, L. Ma, C. Jaye, D. A. Fischer, X. Tong, A. M. Kiss, E. S. Takeuchi, *J. Phys. Chem. C* **2023**, *127*, 7054–7070.
- [57] S. Liu, J. Su, J. Zhao, X. Chen, C. Zhang, T. Huang, J. Wu, A. Yu, *J. Power Sources* **2018**, *393*, 92–98.
- [58] V. Meunier, M. L. De Souza, M. Morcrette, A. Grimaud, *J. Electrochem. Soc.* **2022**, *169*, 70506.
- [59] J. Li, J. Harlow, N. Stakheiko, N. Zhang, J. Paulsen, J. Dahn, *J. Electrochem. Soc.* **2018**, *165*, A2682.
- [60] F. P. McGrogan, S. R. Bishop, Y.-M. Chiang, K. J. Van Vliet, *J. Electrochem. Soc.* **2017**, *164*, A3709.
- [61] H. Zhang, F. Omenya, P. Yan, L. Luo, M. S. Whittingham, C. Wang, G. Zhou, *ACS Energy Lett.* **2017**, *2*, 2607–2615.
- [62] Y. Liu, J. Harlow, J. Dahn, *J. Electrochem. Soc.* **2020**, *167*, 20512.
- [63] J. Li, Z. Zhou, Z. Luo, Z. He, J. Zheng, Y. Li, J. Mao, K. Dai, *Sustain. Mater. Technol.* **2021**, *29*, e00305.
- [64] A. Manthiram, J. C. Knight, S. Myung, S. Oh, Y. Sun, *Adv. Energy Mater.* **2016**, *6*, 1501010.
- [65] J. Kim, H. Lee, H. Cha, M. Yoon, M. Park, J. Cho, *Adv. Energy Mater.* **2018**, *8*, 1702028.
- [66] H.-H. Ryu, K.-J. Park, C. S. Yoon, Y.-K. Sun, *Chem. Mater.* **2018**, *30*, 1155–1163.
- [67] L. Wang, A. Mukherjee, C.-Y. Kuo, S. Chakrabarty, R. Yemini, A. A. Dameron, J. W. DuMont, S. H. Akella, A. Saha, S. Taragin, *Nat. Nanotechnol.* **2023**, 1–11.

Manuscript received: April 9, 2024

Version of record online: June 14, 2024